Paper Physics

Kayla Guyer, Michael Machold, Xiaoyan Tang, Nathan J. Bechle, Junyong Y. Zhu, Biljana M. Bujanovic, Nayomi Z. Plaza, Peter Kitin, Kevin T. Turner and John M. Considine*

Microfibrillated cellulose coatings for biodegradable electronics

https://doi.org/10.1515/npprj-2024-0086
Received November 26, 2024; accepted March 9, 2025;
published online March 24, 2025

Abstract: There is an increasing need for inexpensive biodegradable sensors that can be easily employed in networks such as the Internet of Things. Paper materials are renewable, biodegradable, and sustainable, and thus could be used as substrates for electronic sensors. This work examined two commodity cellulose materials, an envelope paper and a linerboard, as potential substrates. A multistage coating process was developed to create a smooth surface for screen-printing of sensors using inexpensive microfibrillated cellulose. Employing this process, approximately 10 g m^{-2} of microfibrillated cellulose was deposited, enhancing the mechanical performance of the coated materials compared with their uncoated counterparts. Sensors printed on the microfibrillated cellulose-coated substrates had reasonable electronic performance compared with those printed on a polymer substrate. Results indicate that further reducing surface roughness would be helpful for sensor performance.

Keywords: microfibrillated cellulose; coating; electronic sensors; roughness; substrate

Acronyms

BKHP	bleached kraft hardwood pulp
CD	cross-machine direction
CMC	Carboxymethyl cellulose
CNC	cellulose nanocrystals
CNF	cellulose nanofibrils
CNM	cellulose nanomaterials
DIC	digital image correlation
IoT	Internet of Things
LER	line edge roughness
MD	machine direction
MFC	microfibrillated cellulose
NC	nanocellulose
RMS	root mean square
SEM	scanning electron microscopy
UKSP	unbleached kraft softwood pulp

***Corresponding author: John M. Considine**, Forest Products Laboratory, USDA, Forest Service, Madison, WI, USA, E-mail: john.considine@wisc.edu. https://orcid.org/0000-0001-6123-399X
Kayla Guyer, Rose–Hulman Institute of Technology, Terre Haute, IN, USA
Michael Machold and Kevin T. Turner, Mechanical Engineering and Applied Mechanics, University of Pennsylvania, Philadelphia, PA, USA. https://orcid.org/0000-0003-4963-4568 (K.T. Turner)
Xiaoyan Tang, Nathan J. Bechle, Junyong Y. Zhu, Biljana M. Bujanovic, Nayomi Z. Plaza and Peter Kitin, Forest Products Laboratory, USDA, Forest Service, Madison, WI, USA. https://orcid.org/0000-0001-5718-0493 (N.J. Bechle). https://orcid.org/0000-0002-5198-4877 (N.Z. Plaza). https://orcid.org/0000-0002-4717-7108 (P. Kitin)

1 Introduction

The Internet of Things (IoT) is a network of interrelated sensors and devices that provide data to help make decisions in many different fields, and its use has created a demand for large-scale production of sensors. Manufacturing technologies to print sensors can deliver higher volumes at lower cost than conventional fabrication methods. However, current printed sensors are almost exclusively made on engineered polymer substrates that are not renewable nor biodegradable. The long-term vision is to enable a new class of transient biodegradable sensors that can be deployed at high densities, provide data for a specified period, for example, weeks or months, and harmlessly degrade into the environment.

Paper substrates have emerged as a promising platform for printed sensors, providing the mechanical flexibility and strength of engineered polymers while introducing biodegradability. However, paper has high porosity and roughness, which limit the electrical performance of printed electronics fabricated on these substrates. Recent literature has shown that this limiting factor can be mitigated by coating paper substrates to make smoother surfaces with properties that are comparable to engineered polymers.

Dense films of pure cellulose nanomaterials (CNM)-often referred to as nanocellulose (Nc)-have been the focus of recent work due to their increased mechanical strength

and decreased permeability compared to traditional paper. Henriksson et al. were among the first to report the formation and characterization of films from nanocellulose (Henriksson et al. 2008). Subsequent work has been conducted with various CNMs such as cellulose nanocrystals (CNC), cellulose nanofibrils (CNF), and microfibrillated cellulose (MFC). These studies have achieved various levels of permeability to water vapor, grease, and air (Ferrer et al. 2017). Films made from CNF have been utilized as substrates in printed electronics due to their favorable surface properties. The roughness of films made from CNF was found to be 5 nm, which is comparable to polymer films and much less than the roughness of paper (≈5,000 nm) (Huang et al. 2013). Devices made with Nc have included supercapacitors for wearable electronics (Ma et al. 2016), strain sensors (Shao et al. 2018), and flexible transistors (Huang et al. 2013).

Like CNM films, Nc-coated papers have emerged as candidates for printing applications. Hoeng et al. utilized CNC coatings to reduce the surface roughness of cardboard from 66 nm to 3.5 nm,and was able to produce conductive silver lines from inkjet printing (Hoeng et al. 2017). In recent work by Iyer et al. CNF coatings were applied on cardstock for use as substrates in screen-printed electronics where a thin layer of CNF was used to planarize the cardstock surface reducing the roughness from 4,300 nm to 89 nm (Iyer et al. 2022). This roughness is comparable to that of polyimide, a widely used substrate for flexible electronics, with a surface roughness of about 45 nm. The roughness of the substrates was shown to correlate with the quality of printed structures. In addition, these screen-printed structures can leverage the water sensitivity of cellulose-based substrates to form humidity and soil moisture sensors (Iyer et al. 2022). Capacitive structures were printed on the CNF-coated cardstock, and their sensitivity to humidity changes was characterized (Iyer et al. 2022).

The main obstacle impeding the adoption of CNM in flexible electronics is manufacturing. Achieving low surface roughness in large-scale batch-type processes would enable the commercialization of CNF-coated paper. Current Nc coating processes include bar coating at the laboratory scale (Mazega et al. 2022), spray coatings (Hult et al. 2010), and laboratory heat pressing (Iyer et al. 2022). Lavoine et al. examined the barrier and mechanical properties of MFC coatings produced using size press and bar coating processes (Lavoine et al. 2014). The bar coating process resulted in a decrease in air permeance of ~70 %, but it was found that successive wetting and drying cycles reduced the mechanical properties of the coated paper. Challenges with industrial scale manufacturing of CNM coatings include large water content of Nc (Boufi et al. 2016; Brodin and Eriksen 2015), residual stress added to paper during drying, and variations in film quality across a large area.

As interest and development in nanocellulose films grows, primary obstacles to their widespread use remain prohibitive cost and the lack of large-scale manufacturing techniques. The material cost of CNF films is 50–125 times more per unit area than engineered polymers and paper substrates (Hoeng et al. 2016). Alternatively, MFCs are cellulose fibrils that have widths of 50 nm to 1 µm and lengths of tens to hundreds of µm. This material has a larger size factor than CNF, which has fibrils that are around 10 nm wide and hundreds of nm long. MFC is an attractive option for biodegradable coatings due do its lower cost, 16× less expensive than CNF (The University of Maine 2024).

The objective of this work is to develop and employ a biodegradable, inexpensive coating that allows commodity cellulose materials to serve as substrates for electronic sensors. We synthesized a coating composed of 90 % MFC, developed a multi-step coating procedure, evaluated physical and mechanical changes caused by the coating process, screen-printed capacitance sensors on those substrates, and evaluated their resulting electronic performance to determine viability as an electronic sensor.

2 Materials

2.1 Substrates

Two commercial materials were used as substrates, a multiply kraft linerboard and a bleached envelope paper. It should be noted that as commercial materials, the fiber composition, pulping process, and other manufacturing details are not known about these materials. The linerboard likely contained a large portion of recycled material.

2.2 MFC production

A virgin (never dried) bleached kraft hardwood pulp (BKHP) comprising a mixture of birch and maple was provided by Westrock Company as a complimentary sample (Figure 1a). Another virgin unbleached kraft softwood pulp (UKSP), from southern yellow pine, with high lignin content for liner grade was complimentarily obtained from a different US paper company (Figure 1b). The chemical compositions of these two pulps were reported previously (Geng et al. 2024; Zhang et al. 2023) and are listed in Table 1. As received pulps were kept frozen at −16 °C until use.

MFC at two levels of fibrillation were produced from each pulp in a Super Mass Colloider (SMC, Model MKZCA 6-2 J, Disk MDGA 6–80#, Masuko Sangyo Co., Ltd., Japan). The SMC is a stone disk grinder stacked vertically with the top disk stationary. A pulp suspension was fed by gravity into the

hopper mounted on the SMC top disk. As described previously (Hu et al. 2015; Wang et al. 2012), for optimal fibrillation, the pulp suspension consistency was 2 %, disk plate gap was set at –100 µm after loading the pulp suspension (the zero position was when the two disks were in contact before pulp loading), and the bottom disk spinning speed was 1,500 rpm. After the pulp suspension made one pass through

Table 1: Chemical compositions of the two commercial virgin kraft wood pulp samples used in the study.

	K. Lignin (%)	A.S. Lignin (%)	Glucan (%)	Xylan (%)	Mannan (%)
BKHP	0.59 ± 0.15	2.13± 0.01	72.72 ± 1.45	23.14 ± 0.22	0.63 ± 0.00
UKSP	15.88 ± 0.06	3.71± 0.04	53.57 ± 0.47	8.10 ± 0.20	6.28 ± 0.14

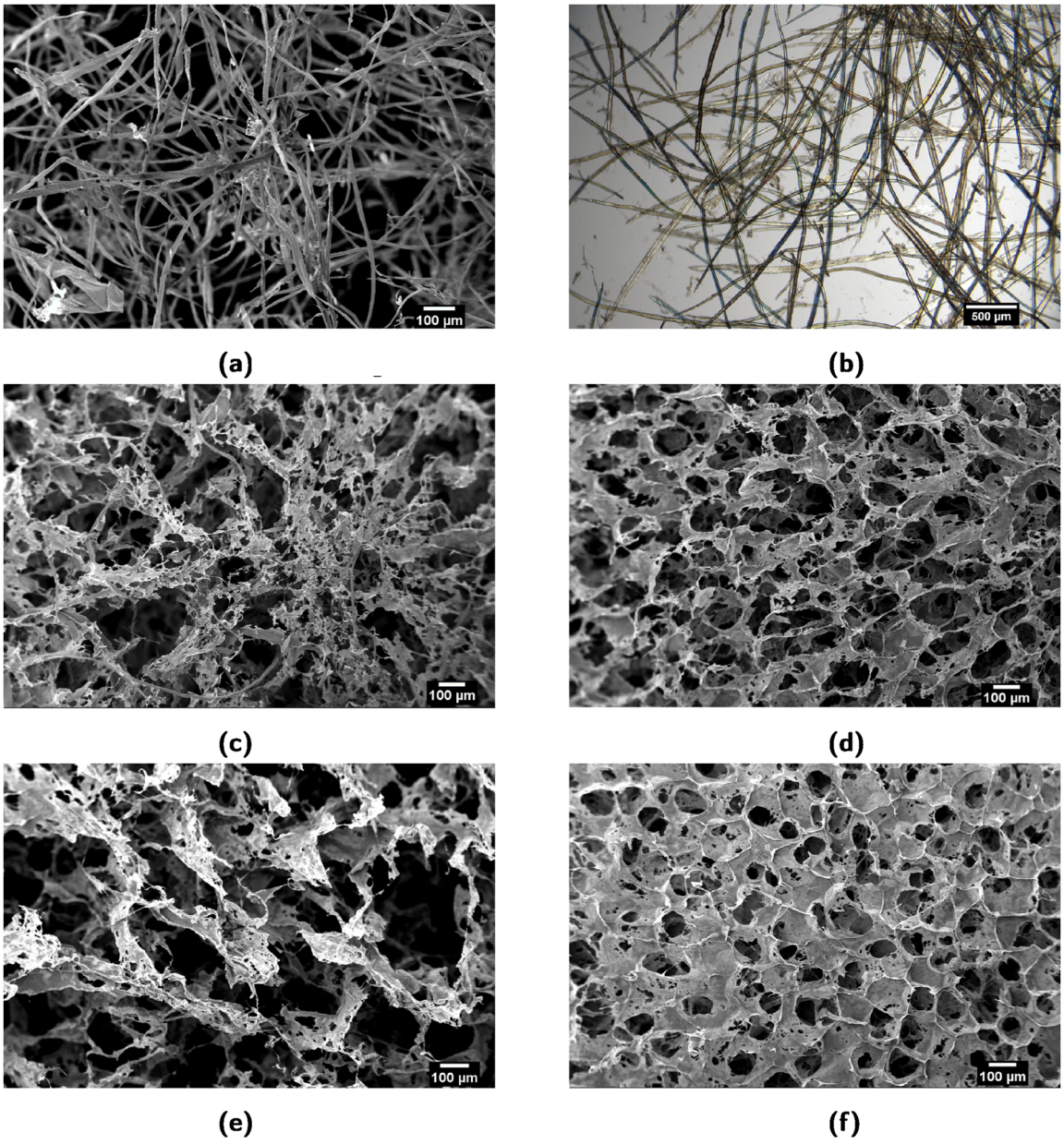

Figure 1: Light microscopy and scanning electron microscopy images of control pulps and after passing through a Super Mass Colloider. (a) SEM image of BKHP as provided. (b) Optical image of UKSP as provided. (c) BKHP after single pass through SMC. (d) UKSP after single pass through SMC. (e) BKHP after four passes through SMC. (f) UKSP after four passes through SMC.

Table 2: Fibrillation energy consumptions for producing the four MFCs. MFC was produced from BKHP and UMFC from UKSP.

Milling passes	MFC-1	MFC-4	UMFC-1	UMFC-4
Milling time (min)	19.53	57.63	21.75	69.35
Specific milling time (min kg^{-1})	97.65	148.8	108.75	170.3
Fiber mass (g)	200	100	200	100
Net energy (kJ)	563	1,151	781	1,698
Specific energy (MJ kg^{-1})	2.82	12.42	3.91	17.56

the SMC, a sufficient amount of MFC (~100 g in oven dry weight) was collected for coating use (Figure 1c and d). The remaining pulp suspension was fed back through the SMC for continued fibrillation for three additional passes (Figure 1e and f) and then collected for later coating use. Energy consumption was determined using the difference of the recorded load and no-load power readings multiplied by the grinding time divided by the pulp mass (oven dry weight) as listed in Table 2.

2.3 Coating preparation

As produced MFC-4 or UMFC-4, denoted generally as MFC going forward, had a composition of 2 % solids and 98 % water. Carboxymethyl cellulose (CMC) powder (Sigma-Aldrich®, Product Number 419338, average Mw ~700,000, degree of substitution 0.80–0.95) was mixed with a small amount of ethanol and stirred to dissolve the powder. Distilled water was added and stirred to create a 1.5 % CMC solution. This solution rested overnight before it was combined with MFC in an Arrow Engineering Mixer, Model#G-5 (Arrow Engineering Company®, Hillside, NJ, USA) for a minimum of an hour to ensure a homogenous mixture for coating. The final MFC-CMC solution was 9 parts MFC to 1 part CMC.

Even at only 2 % solids MFC can be difficult to disperse. CMC has been successfully used as a dispersant for CNMs (Butchosa and Zhou 2014; Mazhari Mousavi et al. 2017) and allowed us to achieve reasonable coating weights.

2.4 Coating process

Specimens of linerboard and envelope paper were obtained and cut to 216 mm × 280 mm. Linerboard specimens were coated with MFC-4 and CMC, and the envelope paper specimens were coated with UMFC-4 and CMC. The color contrast between paper and solution allowed for a visual inspection of the finished samples. The uncoated specimens were then placed felt side down on a large paper towel and the wire side received the coating. Wire side was identified using TAPPI T455, Identification of Wire Side. Strips of 0.5 mm thick silicon screens were placed on the edges of the specimen to add depth to the coating. Approximately 60 cm^3 of the MFC-CMC solution was placed on one edge of the specimen. A BEVS 320/200 coating bar (320 mm long, wet film thickness 200 µm, BEVS® Industry LLC., Guangzhou, China) was placed on the specimen with the edges of the bar on the silicon screens and rolled across the surface of the specimen. The silicon screens prevented the bar from coming in direct contact with the specimen. For initial coatings, the bar was rolled across the surface of the paper multiple times to ensure an even coat. For subsequent coatings, the bar was rolled across the surface only once because more agitation to the specimen resulted in disruption and debonding of previous coatings. The specimen was transferred to a drying rack and placed in a 50 % RH, 23 °C room to partially dry before press drying in order to prevent the coating from adhering to the screen. The amount of time was typically 30–40 min with envelope using shorter drying times. Approximately 2 g m^{-2} dry weight of MFC-CMC was added with each coating and drying step. This process closely aligns with the method employed by Christophliemk et al. (2023), where multiple coatings of 1 g m^{-2} of poly(vinyl alcohol) were applied to achieve targeted barrier properties. They demonstrated that multiple thin layer coatings provided lower oxygen transmission rates than one or two thick layers due to reduction in quantity of pinholes.

2.5 Drying process

The press drying process for the partially dried, MFC-CMC coated specimen used stainless steel screens (100 mesh, wire diameter 0.1 mm, hole size 0.15 mm), 3.2 mm thick steel plates, and a silicon-coated steel sheet to build a barrier between the drying device and the specimen. The specimen was placed in between these materials in order, from bottom to top, steel plate, screen, coated specimen with felt side down, silicon-coated baking sheet, and a steel plate. A schematic of the drying configuration is shown in Figure 2. This sandwich assembly was placed into a hot press heated to 135 °C, and approximately 325 kPa was applied for 5 min. Immediately after removal, the mass of the coated specimen was recorded. After the final coating and cooling, the edges of the specimen were trimmed to remove the portion of the substrate beneath the silicon strips. This drying assembly was designed to provide restraint, ensuring the specimens dried flat, while allowing steam to escape through the screen rather than through the specimen. Layers of MFC-CMC were added until the dry coating weight was approximately 10 g m^{-2}. Given that 2 g m^{-2} dry weight of MFC-CMC was added with each coating (see Section 2.4), it took 5–6 coatings to achieve 10 g m^{-2} of coating.

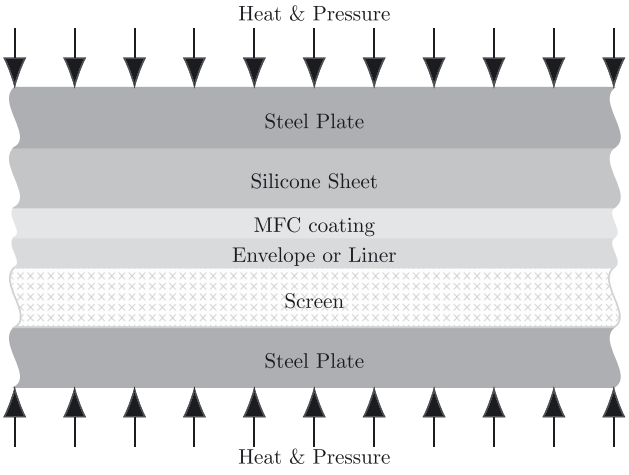

Figure 2: Drying assembly used for each coating step, not to scale.

2.6 Final preparation for testing

Caliper, porosity, and smoothness measurements were conducted after completion of the coating and drying processes. For sheets designated for tensile tests, an optimized random grey level pattern, as described by (Bossuyt 2013), was copied onto the felt side using a Sharp® (Sharp Electronics Corp., Mahwah, NJ) MX-3100N copier.

To assess the effect of the wetting and drying processes on the substrates, each substrate was soaked for 30 min and subsequently dried following the previously described procedure.

Kapton®, a polyimide film, 0.13 mm thick, was used as a reference electrical-grade substrate for printing capacitance sensors.

3 Methods

Coating mixture characteristics were examined with zeta potential measurements. Physical and mechanical properties of the original substrates, redried substrates, and MFC-coated substrates were measured. Mechanical properties were examined to characterize the enhancement or degradation of behavior resulting from the coating process. SEM imaging was used to examine coating thickness and penetration. Printed circuits were characterized with optical imaging and capacitance behavior.

3.1 Zeta potential

Zeta potential and electrophoretic mobility (μ) of aliquots from the coating mixtures were obtained via Phase-analysis of Light scattering (PALS) mode on a NanoBrook Omni dynamic light scattering system (Brookhaven Corp., Holtsville, NY, USA). The instrument is equipped with a 640 nm laser, and the scattering angle of 15° used for PALS. About 2 mL of each MFC coating material (prepared as described in Section 2.3) was loaded into 4 mL cuvettes (BI-SCP) and the electrode assembly (BI-ZEL) was inserted. Bubbles were removed and the cuvette surfaces were thoroughly cleaned to remove any excess material prior to the measurements. Data analysis was performed using the Particle Solutions software (v3.1), where μ was converted to zeta potential values via the Smoluchwski approximation. Each sample was measured five times, and each measurement included 30 cycles. All measurements were performed at 25 °C. Values reported correspond to the mean and standard error. The pH was measured with a Double Junction Waterproof pHTestr™ 30 (Environmental Express Inc., Charleston, South Carolina, USA) and is also reported.

3.2 Physical properties

The physical properties of the coated and uncoated materials were determined with the following techniques and equipment.

- Surface roughness was measured according to TAPPI T 538, Roughness of paper and paperboard, Sheffield Method, using a Technidyne® (Industrial Physics, New Albany, IN USA) Profile/Plus instrument.
- Permeability was measured according to TAPPI T 460, Air resistance of paper (Gurley method) using a Technidyne® (Industrial Physics, New Albany, IN USA) Profile/Plus.
- Grammage was measured according to TAPPI T 410, Grammage for Paper and Paperboard.
- Caliper was measured using an EMVECO® (ABB, Zurich, Switzerland) Model 200A Electronic Thickness Gage.
- Ash was determined according to TAPPI T 211 om-02, Ash in wood, pulp, paper and paperboard: combustion at 525 °C.

Values obtained are listed in Table 5. The ash determination is given only for the original substrates, because the soaked/redried substrates would have the same ash content and the MFC did not contain any inorganic materials. For both of the MFC-coated substrates, the reduced porosity was below the resolution of the instrument.

3.3 Tensile

Tensile experiments employed digital image correlation (DIC) to measure full-field deformations in order to more

Table 3: Technical information about the DIC equipment, set-up, and system.

Parameter	Setting
Technique	Stereo Image Correlation
Cameras	Flir Blackfly S BFS-U3-200S6M
Lens	Computar (Commack, NY) M1614-MP2, 16 mm, f1.4-f16
Lens Filter	Midwest Optical (Palatine, IL) PR032-30.5 Linear Polarizer
Imaging distance	0.356 m
Lighting	White LED, Aputure (Los Angeles, CA) Amaran HR672S
Resolution	2452 × 2056, 12-bit
Noise	0.4 % of dynamic range
Software	MatchID v2024.1.0
Pixel to mm conversion	1 pixel = 0.052 mm
ROI	130 mm × 24 mm
Subset, step	21, 10 (pixels)
Displacement, in-plane resolution	0.033 pixels, 1.7 µm
Strain	
Calculation	Quadratic Quadrilateral
Strain Window	15 data points
VSG, Virtual Strain Gage	161 pixels, 8.40 mm
In-plane Resolution	141 µm m^{-1}

accurately determine modulus and Poisson ratio. Tests were performed on a MTS® Insight 1 820-001-EL test machine (MTS Systems Corp., Eden Prairie, MN, USA) equipped with a MTS® 569327-01 500N load cell. Specimens were 25 mm wide, and gauge length was 178 mm. Gauge length was the same for all specimens and is provided for information only. Grips were 25 mm × 25 mm with a sandpaper surface. Tensile tests were performed in the machine direction (MD), cross-machine direction (CD), and at 45° to MD. DIC hardware and analysis information are given in Table 3.

The loading rate was not consistent for the linerboard–based tensile tests. For those tests, the loading rate was 0.03 mm/s for MD, 0.05 mm/s for CD, and 0.04 mm/s for 45° to MD. Minimal differences in loading rate have a small effect on tensile properties (Gunderson et al. 1988), but the properties of all linerboard-based materials can be compared to assess the effect of the coating process. The image capture rate for the linerboard was 1 Hz. The loading rate for all envelope testing was 0.1 mm/s, and the image capture rate was 2 Hz.

Longitudinal and transverse strains were determined using stereo DIC. Longitudinal strains were used to identify E_{11}, E_{22}, and E_{45^o}. For these calculations we assume that MD and CD are aligned with the 1-direction and 2-direction, respectively. Using the transverse strains, ν_{12} and ν_{21} were identified from the 1-direction and 2-direction tests, respectively.

Strength and failure strain can be determined directly from the load and deformation data. Modulus and energy absorption parameters were calculated by fitting the data with

$$\sigma = C_1 \tanh[C_2(\varepsilon - C_4)] + C_3(\varepsilon - C_4) \quad (1)$$

where σ is applied force per width normalized by grammage (specific stress units), ε is longitudinal strain, and C_i are constants to be fit. Some of the constants have a physical interpretation, e.g., C_2 is a type of yield strength, C_3 is the linear slope of the data near the end of the test, and C_4 is the strain offset to ensure the initial portion of the fit passes through zero strain. After fitting the data, the identified modulus is determined by differentiating Equation (1) and setting $\varepsilon = 0$ as shown in

$$E = C_1 \cdot C_2 + C_3 \quad (2)$$

where E is the initial modulus.

Stiffness transformation was employed to determine shear modulus, G, as described in multiple references, e.g., (Jones 1975), as

$$G = \frac{1}{\left(\frac{4}{E_{45^o}} - \frac{1}{E_{11}} - \frac{1}{E_{22}} + \frac{2\nu_{12}}{E_{11}}\right)} \quad (3)$$

Additionally, Equation (1) can be integrated to determine tensile energy absorption (TEA) to give

$$U = (C_1/C_2)\log[\cosh(C_2(\varepsilon_{\max} - C_4))] + C_3(\varepsilon_{\max} - C_4)^2/2 \quad (4)$$

where U is the specific tensile energy absorption and $\varepsilon_{\max}$ is the failure strain.

3.4 SEM imaging

Pulps and MFC samples in 0.01 wt% aqueous suspension were first observed by bright-field transmission light microscopy without staining with a Nikon® Eclipse Ci microscope (Nikon Corp., Tokyo, Japan). For scanning electron microscopy (SEM) of MFC, we followed the protocol by Zhang et al. (2023). A 5 µL drop of MFC suspension was placed onto a carbon tape, which was mounted on an aluminum stub and then frozen at −20 °C for 1 h. Then the sample was immersed in liquid nitrogen for 1 min and lyophilized in a freeze-drier at 0.133 mbar.

For characterization of the coated surfaces, a 1 cm^2 section of each sample was mounted flat on carbon tape (SPI Supplies, West Chester, PA, USA) to observe the plain

MFC-coated surfaces. For observation of cross-sections, pieces of each sample were sandwiched between two carbon tapes, transversely cut with a razor blade, and were mounted on 90° specimen stubs. The specimens were sputter-coated with gold to enhance conductivity, and SEM images were captured using a Zeiss® Evo 15 (LaB6) Scanning Electron Microscope (Carl Zeiss Microscopy LTD., Oberkochen, Germany) operated at 3–5 kV accelerating voltages.

3.5 Screen printing of circuits

The role of MFC coatings in decreasing the surface roughness of cellulose-based substrates was investigated to determine the suitability of these substrates for screen-printed electronics. Four cellulose-based substrates including linerboard, MFC-coated linerboard, envelope, and MFC-coated envelope were investigated. Kapton®, a polyimide film, which is a widely used polymer substrate in flexible electronics, was used as a reference electrical-grade substrate for printing capacitance sensors. Electronic structures were printed onto the substrates in NovaCentrix HPS-FG77 silver nanoparticle ink (NovaCentrix, Austin, TX, USA) using a HMI MSP–485 semi-automatic screen printer (Hary Manufacturing Inc., Lebanon, NJ, USA). The pattern design consisted of lines 100 µm in width having 7 mm of length spaced in intervals of 250 µm. This design was chosen for use as a capacitive moisture sensor (Iyer et al. 2022). Printed patterns were then annealed at 150 °C for 1 h to solidify and decrease the resistivity of the ink.

3.6 Imaging of printed structures

Substrates with printed patterns were imaged on a Zeiss Axio Imager.A1m microscope (Carl Zeiss Microscopy) using a 10× objective. From microscope images, the line profiles of 1 mm line sections were extracted. Using these line profiles, the average line width of the section was measured. Additionally, line edge roughness (LER) was measured by comparing both line edge profiles to that of a straight line. LER is a common metric to compare the fabrication of electronic structures to designed structures.

Calculation of LER is

$$\mathrm{LER} = \sqrt{\frac{1}{n}\sum_{i=1}^{n}\left(Y_i - Y_{\mathrm{mean}}\right)^2} \tag{5}$$

where LER is dependent on the number of points, n, taken along the profile, the width of the silver line at each point measured from center of the trace, Y_i, and the average width of the silver measured from the center of the line, Y_{mean}.

3.7 Measurement of roughness of printed structures

Out-of-plane geometry of the printed ink, relative to the substrate surface, affects the resistance of the printed pattern and can cause differences between design and fabricated structure performance. A Keyence VK-X3000 confocal laser microscope (Keyence, Osaka, Japan) with a 10× objective was used to record a height map of substrates and printed silver lines. The multi-line root mean square (RMS) roughness of 1 mm sections of the silver lines were measured. To measure this parameter, the average RMS line roughness of 11 lines separated by 4 pixels each was calculated. This measurement was taken at 6 locations on 5 separate samples, resulting in 30 measurements per substrate. Out-of-plane RMS line roughness was calculated by

$$R_q = \sqrt{\frac{1}{m}\sum_{i=1}^{m}\left(Z_i - Z_{\mathrm{mean}}\right)^2} \tag{6}$$

where R_q is dependent on the number of points, m, taken along the profile, the height of the silver line at each point, Z_i, and the average height of the silver line segment, Z_{mean}. The middle line was positioned at the center of the silver line. Multi-line roughness was chosen to evaluate the uniformity across the width of the line as opposed to taking line roughness at only the line center.

3.8 Capacitance measurement

To measure the correlation between the electrical properties of printed structures and line geometry, the capacitance of the interdigitated capacitors was measured for five specimens on each of the five substrates, linerboard, coated linerboard, envelope, coated envelope, and Kapton®. A Hioki IM3536 LCR meter (Hioki E.E. Corporation, Japan) was used to measure the capacitance and phase angle of a wired screen printed capacitor at a frequency of 8 MHz.

4 Results

Despite their valuable and well-understood biodegradable characteristics, paper-based materials have had limited impact within the field of flexible electronics due to their high surface roughness. In this study, we introduce MFC-coated paper as a mechanism to improve the surface roughness for two different mediums. Various properties of the coating, as well as both uncoated and coated substrates, are presented with regards to their impact on the viability of paper-based biodegradable flexible electronics.

4.1 Zeta potential

MFC was prepared for coating by incorporating CMC, a commonly used dispersant, to enhance stability by preventing the agglomeration of MFC particles and improving viscosity homogeneity (Butchosa and Zhou 2014). Zeta potential measurements were used to quantify the impact of incorporating CMC. The mean mobility and the corresponding zeta potential values for the different mixtures are shown in Table 4. Neat MFC or CMC exhibited lower mobility and less negative zeta potentials compared to the formulations with multiple components. Although surface charge and zeta potential can be altered using additives or surfactants, here, all samples had negative zeta potential values, regardless of composition. The magnitude of the zeta potential, often used to assess colloid stability (with absolute values of 30 mV or higher considered stable), varies with pH and typically becomes more positive at lower pH. For cellulose nanoparticles in suspension, the zeta potential can vary between −24 mV and −73 mV from pH 3 to 11 (Anikushin et al. 2022). Previous values for neat MFC and CMC in aqueous media have been reported as −28 ± 2.2 mV in pH 6.5 (Karim et al. 2019), and −35 ± 7 mV at pH 7 (Jung et al. 2022). Our findings are consistent with previous reports, despite pH variations. The addition of CMC, which is generally regarded as a stabilizing agent, has been shown to increase the zeta potential and stability of ovalbumin emulsions (Li et al. 2020) as well as CNF dispersions (Azrak et al. 2021). Moreover, Butchosa and Zhou (2014) reported an irreversible adsorption of CMC onto CNF, an interaction facilitated by the formation of hydrogen bonds between available OH groups in these components. Here, the addition of CMC increased the zeta potential for both bleached and unbleached MFC by 118 % and 64 %, respectively. Bleached MFC, being lignin-free, likely interacts more closely with CMC, enhancing colloid stability, as reflected in the more negative zeta potential compared to that of unbleached MFC. Additionally, the absence of lignin in the bleached MFC likely allowed CMC to interact more closely with cellulose, resulting in higher amounts of negatively charged COO surfaces and hence a more negative zeta potential compared to the unbleached MFC.

Table 4: Mean values of zeta potential, mobilities, and pH of the as-produced suspensions used to coat the substrates. Five replicates were performed. Standard error of the measurements reported in parenthesis.

Material	pH	Mobility (μ/s)/(V/cm)	Zeta potential (mV)
Bleached MFC	5.03	−1.65 (0.10)	−21.07 (1.23)
Unbleached MFC	6.91	−2.03 (0.18)	−25.94 (2.37)
CMC	8.39	−2.21 (0.02)	−28.25 (0.31)
Bleached MFC-CMC	6.34	−3.60 (0.16)	−46.06 (2.08)
Unbleached MFC-CMC	7.05	−3.33 (0.05)	−42.61 (0.69)

4.2 Physical properties

Physical properties for each of the six materials are given in Table 5. Multiple coating cycles were sufficient to increase linerboard grammage by 11 g m^{-2} and envelope by 9 g m^{-2}. The wetting and redrying cycle decreased the linerboard thickness by 48 μm, and the envelope was almost unchanged. Nominal coating thicknesses were 8 μm and 7 μm for the linerboard and envelope, respectively. The coating did not improve the smoothness of the linerboard but did for the envelope. For both substrates, the coating layer filled the pores and reduced the porosity below measurement resolution.

Figures 3 and 4 are SEM images of the control materials and coated materials. Figure 4a shows the difficulty in coating the linerboard, because it is initially more porous, owing to the voids between fibers, requiring the coating to bridge between fibers. Although the coating can fill the pores, the larger gaps between fibers results in a rougher surface. Figure 4b shows a region where the coating was nominally 10 μm thick, while the thickness measurements indicated the average thickness was 7 μm.

Recognizing the difference in magnification in Figure 5, the smoothness of the substrates appeared similar, agreeing with the ranking of Sheffield Smoothness values. After coating, the envelope was much smoother, Figure 6b, than the liner, Figure 6a. The uncoated surface of the envelope is less porous than that of the linerboard, thus less fiber bridging and pore-filling were needed for the coating process, creating less coating defects and an overall smoother surface. Additional coating layers would likely reduce the amount of coating defects (Christophliemk et al. 2023).

4.3 Mechanical properties

The measured mechanical properties are listed in Table 5 and indicate that the coated materials exhibited improved specific strengths and either slight increases or small reductions in specific stiffnesses. The coated materials had greater moduli than the redried materials. E_{22} for the coated materials was greater than for the control materials. The coating produced more isotropic behavior. Some of the reduction for E_{11} can be attributed to release of residual stresses in the 1-direction. As a result, both coated materials had a lower orthotropy ratio (E_{11}/E_{22}) than the control or

Table 5: Summary of physical and mechanical properties for the control and modified materials. Specific tensile properties are provided ($km^2\ s^{-2}$) and represent respective property normalized by density.

Property	Linerboard			Envelope		
	Control	Redried	Coated	Control	Redried	Coated
Grammage ($g\ m^{-2}$)	207	207	218	92	92	101
Thickness (mm)	0.315	0.267	0.275	0.142	0.141	0.148
Ash (%)	1.17	–	–	10.37	–	–
Sheffield Smoothness ($ml\ min^{-1}$)	282	245	328	283	291	257
Gurley Porosity (s)	12.4	24.2	N/A	5.4	5.1	N/A
E_{11} ($km^2\ s^{-2}$)	11.26[a]	9.47	9.71	10.05[a]	7.97	9.39
E_{22} ($km^2\ s^{-2}$)	5.42[a]	4.57	6.40	4.63[a]	2.91	5.02
G_{12} ($km^2\ s^{-2}$)	3.13[a]	2.54	2.74	2.52[a]	1.81	2.55
ν_{12}	0.23[a]	0.44	0.62	0.23[a]	0.57	0.50
E_{11}/E_{22}	2.80[a]	2.07	1.52	2.20[a]	2.74	1.87
$\sigma_{11}^{max} \times 10^3$ ($km^2\ s^{-2}$)	67.94[a]	69.45	71.67	65.22[a]	53.56	68.01
$\sigma_{22}^{max} \times 10^3$ ($km^2\ s^{-2}$)	30.67[a]	35.37	44.35	25.43[a]	21.64	35.81
TEA_{11} ($km^2\ s^{-2}$)	N/A	0.486	0.467	N/A	0.444	0.586
TEA_{22} ($km^2\ s^{-2}$)	N/A	0.514	0.474	N/A	0.361	0.343

[a]indicates data from (Considine et al. 2011) (9).

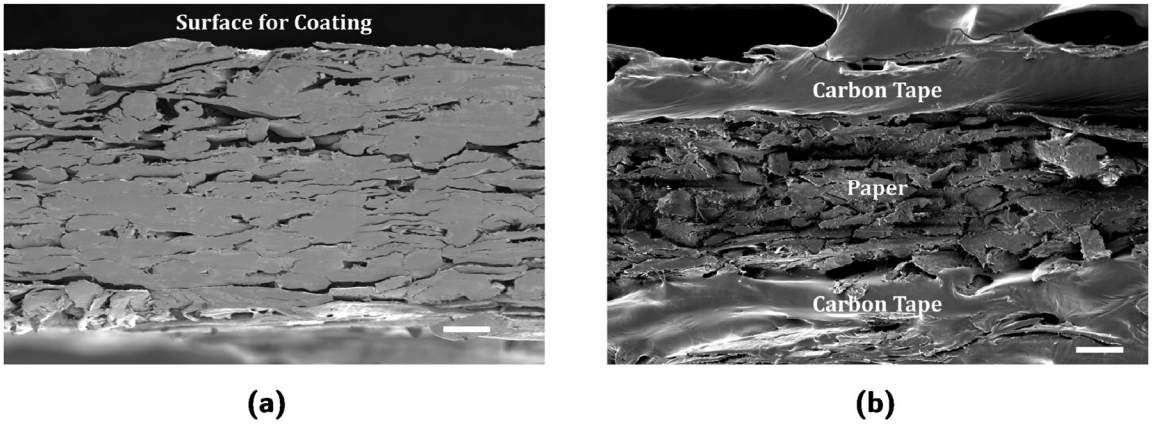

Figure 3: Cross section SEM images for each substrate without coating. Scale bars are 50 µm. (a) Linerboard. (b) Envelope.

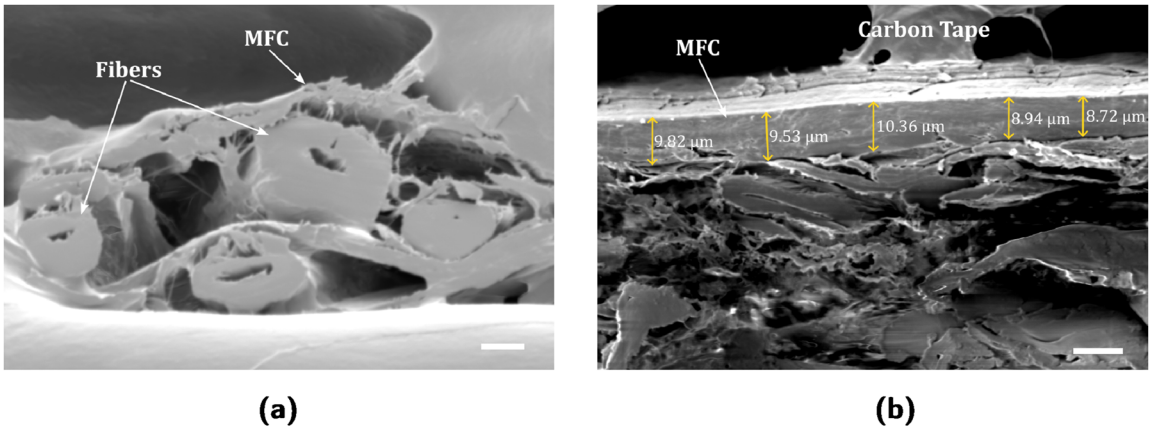

Figure 4: Cross section SEM images for each substrate with coating. Scale bars are 10 µm. (a) Linerboard. (b) Envelope.

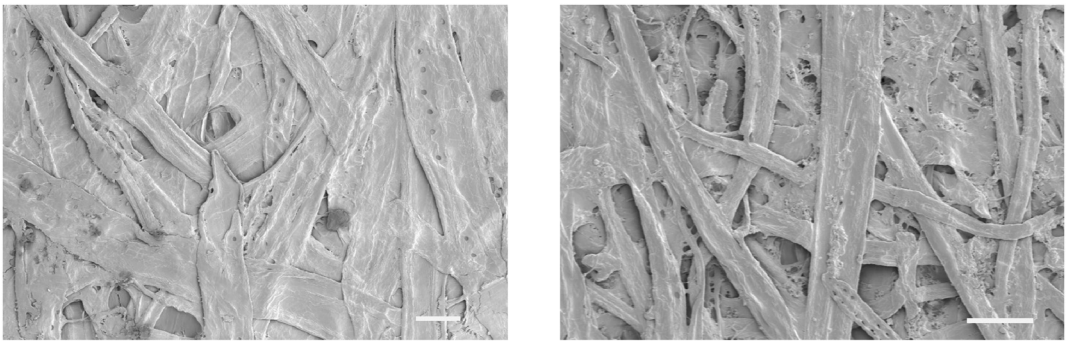

Figure 5: SEM images for the plane views for each substrate without coating. Scale bars are 50 μm. (a) Linerboard. (b) Envelope.

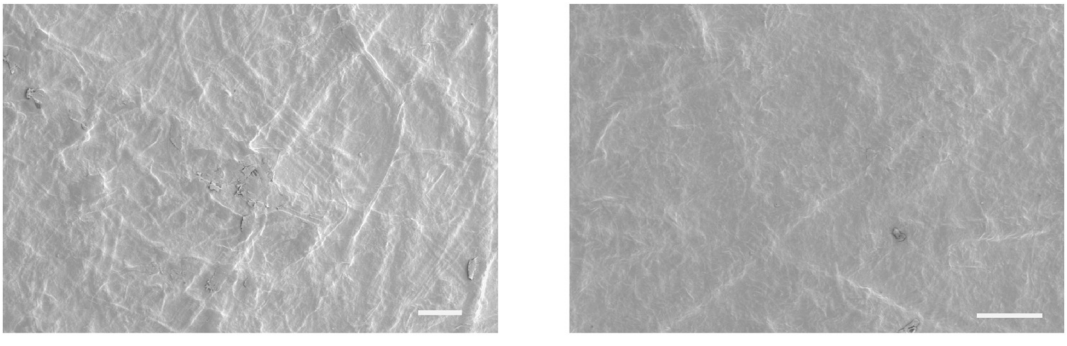

Figure 6: SEM images for the plane views for each substrate with coating. Scale bars are 50 μm. (a) Linerboard. (b) Envelope.

redried materials. As expected, strength was improved more for the 2-direction $(\sigma_{22}^{\max})$ than for the 1-direction. Increased specific strength with MFC coating is in contrast with results from Lavoine et al. (2014) who found a reduction in specific strength when bar coating 14 g m^{-2} MFC on a 41 g m^{-2} base paper; no pulp identification was given in their work, except that it was unbleached. Their reduction of specific tensile strength as compared with our increased specific strength is likely related to the different substrates employed than differences in coating and coating processes. Figure 7 provides a graphical representation of the 2D tensor transformation of the stiffnesses using

$$Q_{11} = \frac{E_{11}}{1 - \nu_{12}\nu_{21}} \qquad Q_{22} = \frac{E_{22}}{1 - \nu_{12}\nu_{21}}$$
$$Q_{12} = \frac{\nu_{21}E_{11}}{1 - \nu_{12}\nu_{21}} = \frac{\nu_{12}E_{22}}{1 - \nu_{12}\nu_{21}} \qquad Q_{66} = G_{12} \tag{7}$$

The area of the polar plots is one measure of material performance; the larger the area, the better the performance (Baum 1987). The polar stiffness plots of the redried materials fit within the control substrates. Coating increased the area of the polar plot relative to the control materials. This indicates that the coating process increased the stiffness of the control substrates by overcoming the stiffness decrease associated with wetting and drying.

Figure 7a and b shows the changes in [Q] for each material. In each case [Q] was improved from both the control substrate and soaked substrate.

4.4 Printed circuits and performance

The geometry of capacitor lines is known to affect the electrical behavior of capacitors by increasing resistance and creating discontinuities (Iyer et al. 2022). Figure 8 shows the screen printed capacitors on uncoated and coated substrates using a 10× objective on an optical microscope. The silver lines conformed to the surface of the substrates, filling pores and surface low regions. Significant nonuniformity of the lines was apparent for the uncoated materials because both the edge of the lines were rough and the surface of the lines showed underlying fibers. MFC-coated substrates (Figure 8c and e) were more uniform.

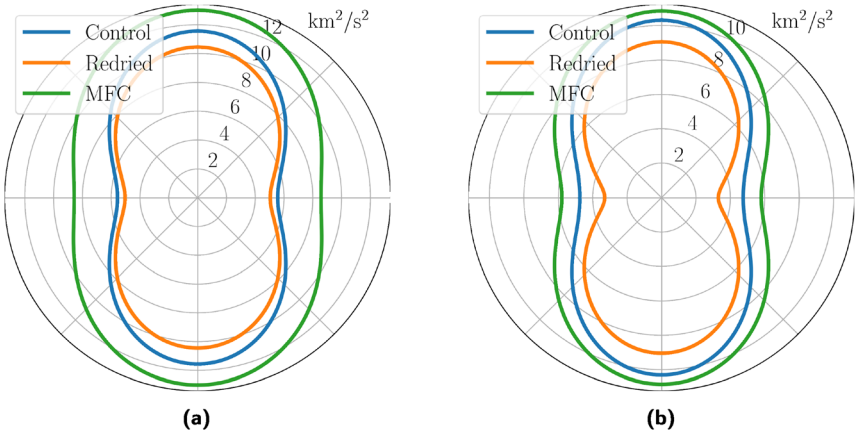

Figure 7: Polar *Q* plots for the six materials. (a) Liner. (b) Envelope.

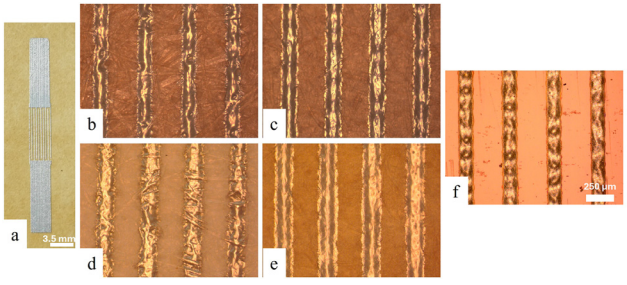

Figure 8: Optical images of capacitor on different substrates. (a) Complete capacitor image on linerboard. (b) 10× image for capacitor on linerboard. (c) 10× image for capacitor on MFC-coated linerboard. (d) 10× image for capacitor on envelope. (e) 10× image for capacitor on MFC-coated envelope. (f) 10× image for capacitor on Kapton®.

For each substrate, line width and LER (Equation (5)) were quantified from edge profiles of 1 mm long lines. Figure 9 is a violin plot that indicates that there is no statistical difference between the line width of coated and uncoated materials. A violin plot shows data distribution and density. The center horizontal line of a violin plot denotes the median of the data distribution. The upper and lower horizontal lines denote the upper and lower quartile ranges for the data. The width of the outer curved lines represent the data distribution as determined from kernel density distribution (KDE). KDE is a statistical technique that is used to calculate the probability density function. The differences observed in the linerboard and envelope ranges are linked to the screen printer settings used and the difference in thickness between the two substrates. The linerboard and envelope substrates were printed on different days, and the printer settings were not identical but adjusted to optimize completeness of prints, which is affected by level of ink spreading and infiltration on each unique substrate. Additionally, sheet-level unevenness in coating thickness can lead to line width differences across sensors printed in the same batch due to a screen printer snap off distance that is not the same across the whole substrate. Generally, the coated materials had lower LER means and ranges (Figure 9) than the uncoated materials.

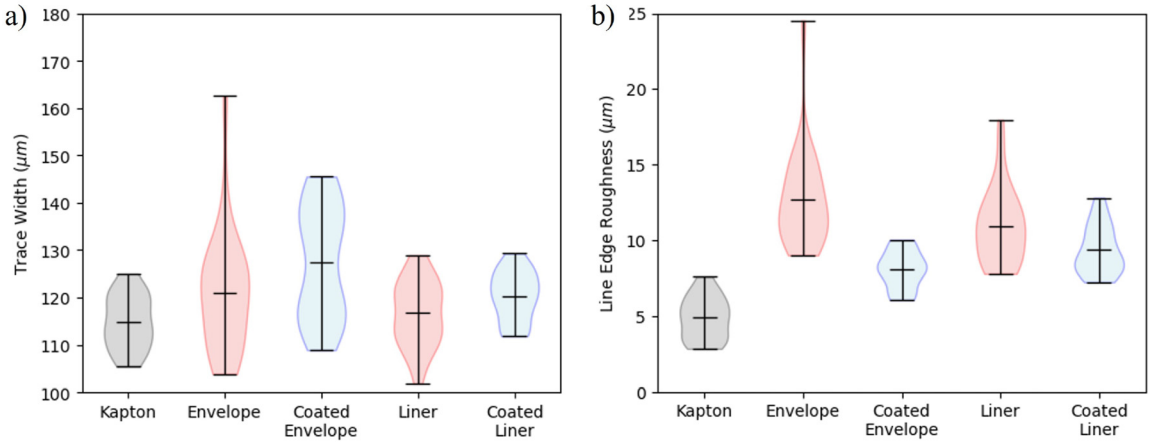

Figure 9: Dimensions of silver screen printed lines extracted from microscope images. (a) Average line width across length of 1 mm. (b) LER of line edges across length of 1 mm where n = 25. Error bars indicate maximum and minimum value. Mean of data points is marked.

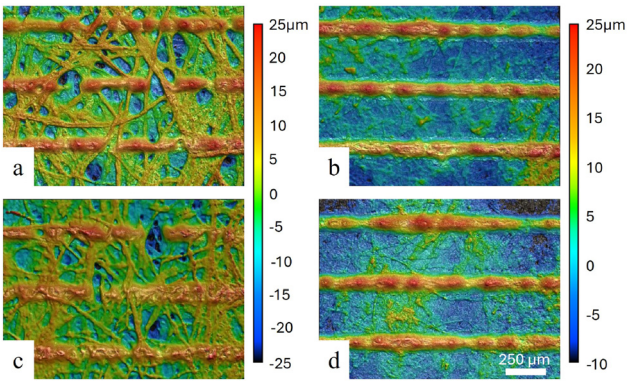

Figure 10: Height maps of silver ink printed on substrates measured using confocal laser microscopy. Images of substrates including (a) linerboard, (b) MFC-coated linerboard, (c) envelope paper and (d) MFC-coated envelope paper.

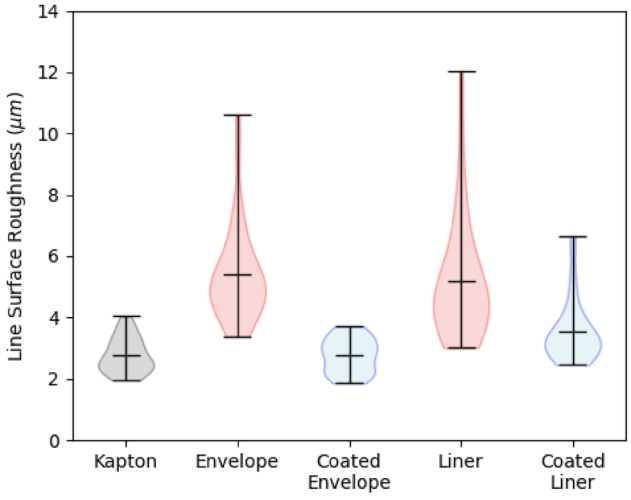

Figure 11: Multi-line surface roughness for five substrates measured with confocal laser microscopy (n = 30).

Table 6: Average and standard deviation of line roughness for each substrate measured with confocal laser microscopy. Length of each line was 1 mm (n = 30).

	RMS (µm)
Kapton®	2.77 (0.57)
Envelope	5.41 (1.60)
MFC Envelope	2.76 (0.57)
Linerboard	5.20 (2.05)
MFC Linerboard	3.54 (1.03)

These differences were statistically different at the 95 % confidence level for the envelope materials. MFC-coated liner did not have statistically significant lower LER than uncoated liner. Kapton® had statistically lower LER than all materials. Smaller LER indicated less spreading of the ink and reduced infiltration. A small LER leads to resistance of lines that is constant along the length of the capacitive finger.

Line width and LER capture the 2D geometry of the silver lines. Confocal microscopy was used to examine the topography of those lines. Figure 10a and c shows how the rough, porous surface of uncoated cellulose substrates leads to height variation in the silver lines. Coated substrates have significantly less surface roughness, as shown in Figure 10b and d, resulting in more uniform line heights.

Differences in topography were characterized from the confocal laser images with Equation (6) using lengths of 1 mm. Those results are shown in Figure 11 and Table 6. Uncoated linerboard and envelope paper have roughness of 5.20 and 5.41 µm, respectively. This high roughness is caused by variation of thicknesses of the cellulose fibers. Additionally, the standard deviation for these substrates is 1.60 and 2.05 µm. The high variance is attributed to discontinuities in silver ink from large pores that do not allow silver ink deposition.

MFC-coated linerboard had a decreased average value and standard deviation for multi-line roughness compared to the uncoated substrate. However, the MFC coating was not thick enough to cover all microfibers of the underlying substrate. This led to some lines with discontinuities or greater height in areas where exposed microfibers intersected the silver ink. MFC-coated envelope paper had the lowest multi-line roughness with a value of 2.76 µm and a standard deviation of 0.57 µm. These values are comparable to the multi-line roughness of Kapton®, which had an average value of 2.77 µm and a standard deviation of 0.57 µm. Minimally exposed cellulose microfibers led to a lower line roughness compared to the coated linerboard.

We used Tukey's honestly significant difference test to perform pairwise comparisons of each of the five materials in Figure 11. Using a 95 % confidence interval, the results indicated that Kapton®, coated envelope, and coated liner were not statistically different. This result demonstrates that the MFC coating effectively reduced surface roughness, rendering the surface smoothnesses of the coated materials comparable to that of Kapton®. The uncoated materials, envelope and liner, had line surface roughnesses that were not statistically different from each other.

The behavior of the screen-printed capacitance sensors, shown in Figure 8, was characterized with an 8 MHz AC frequency. The capacitance and phase angle behavior is shown in Figure 12. The range of capacitance values was larger for uncoated materials than for coated materials, which corresponds to the topographical heterogeneity as shown in Figure 11. Discontinuities cause inactive capacitor

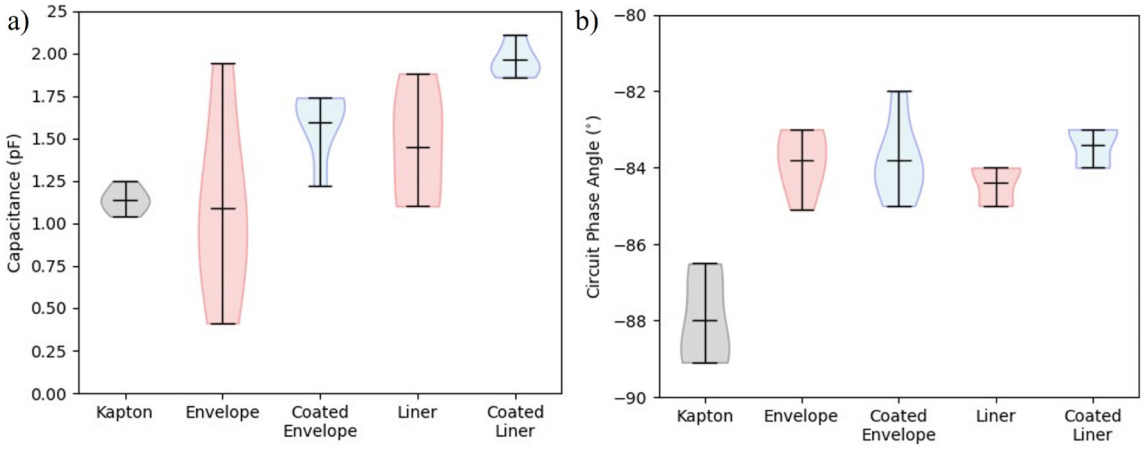

Figure 12: Electrical properties at 8 MHz of sensors screen printed on cellulose substrates. (a) Capacitance of sensors on cellulose substrates. (b) Phase angle of screen-printed sensors on cellulose substrates. Five replicates were examined for each substrate.

fingers that drastically decrease the capacitance, whereas lower substrate roughness leads to consistent electrical properties. The phase angle of all the substrates was below −80° (Figure 12), which indicates that the printed sensors were dominated by capacitance but exhibited resistance attributed to current leakage through the cellulose substrates. Coating had no statistical effect on phase angle. When compared to the capacitance of prints on polyimide, the variance of prints on coated substrates approached that of prints on the engineered polymer. The range of capacitance of structures printed on polyimide was lower due to the higher dielectric constant of the cellulose substrates that absorb more moisture in the tested environment of 50%RH and 23 °C. When comparing the performance of prints on the cellulose substrates to the polyimide, the MFC-coated substrates resulted in ink structures with consistent capacitance similar to those printed on polyimide, whereas the uncoated substrates resulted in high variance in capacitance linked to their higher roughness.

5 Discussion

This work focused on using MFC as a coating for inexpensive commodity materials to create biodegradable sensors. MFC was chosen as the primary coating component to create an economical alternative to coatings based on CNF. The coating formulation (Section 2.3) and coating and drying processes (Sections 2.4 and 2.5) improved tensile specific strength, marginally reduced specific stiffness, and improved Sheffield smoothness (Table 5). The topography of the sensors printed on MFC-coated materials was statistically similar to those printed on Kapton® (Figure 11). The range of capacitance values is an indicator of sensor integrity. Because the variation of capacitance for Kapton® and the MFC-coated materials was similar (Figure 12), we have confidence that MFC can be used to provide an acceptable surface for many applications. Iyer et al. (Iyer 2023; Iyer et al.) found that CNF could also produce a surface comparable to Kapton® for similar sensors, albeit at a higher expense.

Sensor performance may be improved by further reducing coating roughness. The envelope material initially has a smoother surface than linerboard, which helped create a smoother final surface when a similar coating amount was applied, as shown in Figure 6. Potential options exist to further improve smoothness, such as increased coating weight, or a secondary coating like CNF, which can flow and fill surface troughs. Although biodegradability is important, a thin non-conductive coating, e.g., epoxy, silica, or polyurethane, may improve electrical performance sufficiently to increase the number of applicable markets.

We previously used similar printed capacitors as moisture sensors on a different type of coated paper substrates (Zaccarin et al. 2024). We plan to use the current substrates for sensing applications and will characterize the moisture absorption and distribution in the substrates in future work.

6 Conclusions

The objective of this work was to develop and employ a biodegradable, inexpensive coating so that commodity cellulose materials can be used as substrates for electronic sensors. To that end, two commodity materials, linerboard and envelope paper, were coated with MFC and printed with

silver capacitance sensors. The electrical performance of the sensors was sufficient for some applications, but further improvement would enable broader applications.

The roughness of the linerboard was greater than that of the envelope paper. We employed a multi-stage coating process to deposit about 10 g m^{-2} of MFC, which reduced the surface roughness of both substrates, however, the coated linerboard remained rougher than the coated envelope. The mechanical performance of the coated materials was marginally improved by the coating process.

The performance of the sensors was affected by surface roughness of the coated materials that, in turn, produced roughness in the sensors and reduced their performance. Additional coating layers may have improved the sensors on the linerboard. This work demonstrated a route to create inexpensive, biodegradable substrates for electronic sensors in a manner that maintains substrate mechanical integrity.

Research ethics: Not applicable.
Informed consent: Not applicable.
Author contributions: The authors have accepted responsibility for the entire content of this manuscript and approved its submission.
Use of Large Language Models, AI and Machine Learning Tools: None declared.
Conflict of interest: The authors state no conflict of interest.
Research funding: This work was partially supported by financial assistance from the USDA Forest Service through the Private–Public Partnership for Nanotechnology in the Forestry Sector (P3Nano) under grant 23-JV-11111122-020.
Data availability: The raw data can be obtained on request from the corresponding author.

References

Anikushin, B.M., Lagutin, P.G., Kanbetova, A.M., Novikov, A.A., and Vinokurov, V.A. (2022). Zeta potential of nanosized particles of cellulose as a function of pH. *Chem. Tech. Fuels Oils* 57: 913–916, https://doi.org/10.1007/s10553-022-01328-0.

Azrak, S.M.E.A., Gohl, J.A., Moon, R.J., Schueneman, G.T., Davis, C.S., and Youngblood, J.P. (2021). Controlled dispersion and setting of cellulose nanofibril – carboxymethyl cellulose pastes. *Cellulose* 28: 9149–9168, https://doi.org/10.1007/s10570-021-04081-5.

Baum, G.A. (1987) Polar diagrams of elastic stiffness: effect of machine variables. In: *Proceedings: 1987 international paper Physics conference*, pp. 161–166.

Bossuyt, S. (2013) Optimized patterns for digital image correlation. In: *Proceedings of the 2012 annual conference on experimental and applied mechanics, Volume 3: imaging methods for novel materials and challenging applications*. Society for Experimental Mechanics, Springer, pp. 239–248.

Boufi, S., González, I., Delgado-Aguilar, M., Tarrès, Q., Àngels Pèlach, M., and Mutjé, P. (2016). Nanofibrillated cellulose as an additive in papermaking process: a review. *Carbohydr. Polym*. 154: 151–166, https://doi.org/10.1016/j.carbpol.2016.07.117.

Brodin, F.W. and Eriksen, O. (2015). Preparation of individualised lignocellulose microfibrils based on thermomechanical pulp and their effect on paper properties. *Nord. Pulp Paper Res. J.* 30:443–451, https://doi.org/10.3183/npprj-2015-30-03-p443-451.

Butchosa, N. and Zhou, Q. (2014). Water redispersible cellulose nanofibrils adsorbed with carboxymethyl cellulose. *Cellulose* 21: 4349–4358, https://doi.org/10.1007/s10570-014-0452-7.

Christophliemk, H., Bohlin, E., Emilsson, P., and Järnström, L. (2023). Surface analyses of thin multiple layer barrier coatings of poly(vinyl alcohol) for paperboard. *Coatings* 13: 1489, https://doi.org/10.3390/coatings13091489.

Considine, J., Vahey, D., Evans, J., Turner, K., and Rowlands, R. (2011). Evaluation of strength-controlling defects in paper by stress concentration analyses. *J. Compos. Mater*. 46: 1323–1334, https://doi.org/10.1177/0021998311418262.

Ferrer, A., Pal, L., and Hubbe, M. (2017). Nanocellulose in packaging: advances in barrier layer technologies. *Ind. Crop. Prod.* 95: 574–582, https://doi.org/10.1016/j.indcrop.2016.11.012.

Geng, J., O'Dell, J., Stark, N., Kitin, P., Zhang, X., and Zhu, J.Y. (2024). Microfibrillated cellulose (MFC) barrier coating for extending banana shelf life. *Food Hydrocolloids* 150: 109671, https://doi.org/10.1016/j.foodhyd.2023.109671.

Gunderson, D.E., Considine, J.M., and Scott, C.T. (1988). The compressive load-strain curve of paperboard: rate of load and humidity effects. *J. Pulp Pap. Sci*. 14: J37–J41.

Henriksson, M., Berglund, L.A., Isaksson, P., Lindström, T., and Nishino, T. (2008). Cellulose nanopaper structures of high toughness. *Biomacromolecules* 9: 1579–1585, https://doi.org/10.1021/bm800038n.

Hoeng, F., Denneulin, A., and Bras, J. (2016). Use of nanocellulose in printed electronics: a review. *Nanoscale* 8: 13131–13154, https://doi.org/10.1039/C6NR03054H.

Hoeng, F., Bras, J., Gicquel, E., Krosnicki, G., and Denneulin, A. (2017). Inkjet printing of nanocellulose–silver ink onto nanocellulose coated cardboard. *RSC Adv.* 7: 15372–15381, https://doi.org/10.1039/C6RA23667G.

Hu, C., Zhao, Y., Li, K., Zhu, J.Y., and Gleisner, R. (2015). Optimizing cellulose fibrillation for the production of cellulose nanofibrils by a disk grinder. *Holzforschung* 69: 993–1000, https://doi.org/10.1515/hf-2014-0219.

Huang, J., Zhu, H., Chen, Y., Preston, C., Rohrbach, K., Cumings, J., and Hu, L. (2013). Highly transparent and flexible nanopaper transistors. *ACS Nano* 7: 2106–2113, https://doi.org/10.1021/nn304407r.

Hult, E.-L., Iotti, M., and Lenes, M. (2010). Efficient approach to high barrier packaging using microfibrillar cellulose and shellac. *Cellulose* 17: 575–586, https://doi.org/10.1007/s10570-010-9408-8.

Iyer, G.M. (2023). *Design, characterization and fabrication of low-cost, passive, and biodegradable sensors for precision agriculture*, PhD thesis. University of Pennsylvania, Available at: https://repository.upenn.edu/handle/20.500.14332/59413.

Iyer, G.M., Machold, M., Zaccarin, A.-M., Olsson, R.H., and Turner, K.T. Biodegradable nanocellulose coated paper for screen printed electronics. To be submitted.

Iyer, G.M., Zaccarin, A.-M., Olsson, R.H., and Turner, K.T. (2022) Fabrication and characterization of cellulose-based materials for biodegradable soil moisture sensors. In: *2022 IEEE sensors*, pp. 1–4.

Jones, R.M. (1975). *Mechanics of composite materials*. Taylor & Francis, London.

Jung, M., Kim, J., Jung, S., Kim, Y., Bang, J., Yeo, H., Choi, I.-G., and Kwak, H.W. (2022). pH-responsive hydrogels of carboxymethyl cellulose and polyethyleneimine for efficient removal of ionic dye molecules. *BioResources* 17: 5785–5802, https://doi.org/10.15376/biores.17.4.5785-5802.

Karim, Z., Svedberg, A., Lee, K.-Y., and Khan, M.J. (2019). Processing-structure-property correlation understanding of microfibrillated cellulose based dimensional structures for ferric ions removal. *Sci. Rep*. 9: 10277, https://doi.org/10.1038/s41598-019-46812-6.

Lavoine, N., Desloges, I., Khelifi, B., and Bras, J. (2014). Impact of different coating processes of microfibrillated cellulose on the mechanical and barrier properties of paper. *J. Mater. Sci*. 49: 2879–2893, https://doi.org/10.1007/s10853-013-7995-0.

Li, Z., Kuang, H., Yang, J., Hu, J., Ding, B., Sun, W., and Luo, Y. (2020). Improving emulsion stability based on ovalbumin-carboxymethyl cellulose complexes with thermal treatment near ovalbumin isoelectric point. *Sci. Rep*. 10: 3456, https://doi.org/10.1038/s41598-020-60455-y.

Ma, L., Liu, R., Niu, H., Zhao, M., and Huang, Y. (2016). Flexible and freestanding electrode based on polypyrrole/graphene/bacterial cellulose paper for supercapacitor. *Comp. Sci. Technol.* 137: 87–93, https://doi.org/10.1016/j.compscitech.2016.10.027.

Mazega, A., Tarrés, Q., Aguado, R., Pèlach, M.A., Mutjé, P., Ferreira, P.J.T., and Delgado-Aguilar, M. (2022). Improving the barrier properties of paper to moisture, air, and grease with nanocellulose-based coating suspensions. *Nanomaterials* 12: 3675, https://doi.org/10.3390/nano12203675.

Mazhari Mousavi, S.M., Afra, E., Tajvidi, M., Bousfield, D.W., and Dehghani-Firouzabadi, M. (2017). Cellulose nanofiber/carboxymethyl cellulose blends as an efficient coating to improve the structure and barrier properties of paperboard. *Cellulose* 24: 3001–3014, https://doi.org/10.1007/s10570-017-1299-5.

Shao, C., Wang, M., Meng, L., Chang, H., Wang, B., Xu, F., Yang, J., and Wan, P. (2018). Mussel-inspired cellulose nanocomposite tough hydrogels with synergistic self-healing, adhesive, and strain-sensitive properties. *Chem. Mater*. 30: 3110–3121, https://doi.org/10.1021/acs.chemmater.8b01172.

The University of Maine (2024). Order nanocellulose, https://umaine.edu/pdc/nanocellulose/order-nanocellulose/ (Accessed 22 August 2024).

Wang, Q.Q., Zhu, J.Y., Gleisner, R., Kuster, T.A., Baxa, U., and McNeil, S.E. (2012). Morphological development of cellulose fibrils of a bleached eucalyptus pulp by mechanical fibrillation. *Cellulose* 19: 1631–1643, https://doi.org/10.1007/s10570-012-9745-x.

Zaccarin, A.-M., Iyer, G.M., Olsson, R.H., and Turner, K.T. (2024). Fabrication and characterization of soil moisture sensors on a biodegradable, cellulose-based substrate. *IEEE Sens. J.* 24: 7235–7243, https://doi.org/10.1109/JSEN.2023.3299430.

Zhang, X., Kitin, P., Agarwal, U.P., Gleisner, R., and Zhu, J.Y. (2023). Characterizing lignin-containing microfibrillated cellulose based on water interactions, fibril properties, and imaging. *Carbohydr. Polym*. 316: 120996, https://doi.org/10.1016/j.carbpol.2023.120996.